High-Q resonances in periodic photonic structures

Kaili Sun [ORCID],[1] Wei Wang,[2] and Zhanghua Han [ORCID][1,*]

[1]*Shandong Provincial Key Laboratory of Optics and Photonic Devices, Center of Light Manipulation and Applications,*
School of Physics and Electronics, Shandong Normal University, Jinan 250358, China
[2]*College of Physics, Sichuan University, Chengdu 610064, China*

The support of high-Q resonances in all-dielectric nanostructures are necessary for the enhancement of light-matter interactions. By introducing some perturbations into periodic structures to enable an engineered coupling between the supported bound modes and the exterior environment, quasibound modes can consequently be achieved. However, the nature of those modes is still in need of clear investigation. In this work, we employ two geometrically similar binary gratings and demonstrate with both numerical and experimental results that two fundamentally different bound modes may lie behind the high-Q resonances reported in the literature: the bound state in the continuum (BIC) and the guided modes in subwavelength photonic lattices. These two modes have distinct dependences of the Q factor on the wave vector and when they are converted into quasibound (leaky) modes, the same behaviors are retained. We find that only those high-Q resonances with the predecessor of guided modes have robust Q factors over a large range of wave vectors and frequencies, which suggests the high tunability of resonances with comparable Q values by the incident angle. In contrast, the BIC provides more versatility for dealing with optical resonances with both high-Q factors and exotic polarizations. These findings correct the general misunderstanding of the origin of high-Q resonances in periodic photonic structures and will significantly broaden the landscape of all-dielectric nanophotonics.

I. INTRODUCTION

In recent years, all-dielectric nanostructures have garnered significant attention due to their unique optical properties, e.g., supporting multiple exotic resonances of both the electric and magnetic types, which suggest a large variety of potential applications across various domains [1]. Particularly, the ultralow absorption loss has prompted a continuing exploration of all-dielectric micro/nanostructures supporting various physical mechanisms for achieving light-matter interactions at different intensities [2]. However, it is known that the strength of light-matter interactions occurring in the near field can be indirectly characterized by the quality factor (Q factor) of the far-field resonance, as the latter is inherently associated with the maximum enhancement of local electric field [3]. Compared to the plasmonic counterpart of resonances in the metallic nanostructures, all-dielectric nanostructures support resonances with a relatively large modal field in the volume of dielectric components, making it necessary to design high-Q resonance to achieve a large local electric field. The most widely used design strategy to this goal, although somewhat obscure, is to start with some well-confined bound modes (BMs), which exhibit infinite-Q factors (i.e., zero linewidth) due to their inability to radiate into free space. Through some intentional geometric perturbations or modified incident conditions, these BMs can be transformed into quasi-BMs with the possibility of being coupled with

external radiation. One typical example of the BMs that has been extensively exploited in recent years is the bound state in the continuum (BIC) [4–6], which was initially introduced in quantum mechanics [7] and has subsequently found widespread applications in optics [8], acoustics [9], and other physical fields. Although conventional BICs cannot be accessed from free space, they can be engineered into quasi-BICs (QBICs) with high-Q factors. For example, by introducing some geometric perturbations into a photonic system supporting the symmetry-protected BIC (SP-BIC), the original eigenmode with strict antisymmetric distribution can be slightly perturbed, enabling a small yet nonzero overlap with the external plane waves and giving rise to the formation of QBICs [4]. This important feature has led to its extensive applications in molecular fingerprint retrieval [10], thermal emitters [11,12], biosensors [13,14], nonlinear optics [15,16], and so on. Although the interaction of multiple localized modes in a single dielectric nanostructure can also give rise to BIC/QBIC modes [17], the Q factor is not high ($Q < 10^3$). Therefore, periodic array structures that support nonlocal QBIC modes have become preferred for achieving ultrahigh-Q factors. A surging number of papers appear every year reporting the realization of high-Q resonances based on periodic structures; however, we noticed from the literature that when people work on the high-Q resonances supported by periodic structures with geometric perturbations, they tend to classify all of them as QBIC without thinking seriously about the origin. However, for some cases, when the geometric perturbation vanishes, the high-Q resonances may restore to other infinite-Q modes other than BIC. In this situation, a clear and

*zhan@sdnu.edu.cn

comprehensive investigation of the underlying physics behind those high-Q resonances is still missing.

In this work, we reveal that beyond the concept of BIC, another type of BM can also be engineered to achieve high-Q resonances. It is the guided modes (GMs) type, which has been well described in many optics textbooks but has received less attention in all-dielectric nanophotonics. Noteworthy, apart from regular optical waveguides, many subwavelength photonic lattices can also support well-confined GMs [18]. A typical example of such kind of lattices is a high refractive index photonic crystal slab (PCS) [19] supporting a series of GMs which are completely confined within the slab layer. When some period-increasing perturbations are introduced into the unit cell of the periodic structures, the first Brillouin zone (FBZ) shrinks, leading to the flipping of the GM dispersion from below the light line to be above it and the generation of new high-Q resonances, which we refer to as quasi-GMs (QGMs) [20] hereinafter. Compared to the QBICs, the QGMs are expected to exhibit different behaviors. The predecessor GMs exhibit infinite-Q factors over a large spectral band and a large range of wave vectors, e.g., the dispersion of the GMs extends to infinite wave vectors for an optical waveguide or to the entire FBZ for a periodic photonic lattice. As a result, the QGMs exhibit robust Q factors across a large proportion of the FBZ, i.e., the Q factors remain weakly affected by the change of wave vector. Furthermore, the QGMs can also offer the same advantages as the QBICs with an inverse decay rate as a function of the perturbation magnitude. From the perspective of topological nature, the BIC point exhibits a vortex center carrying an integer topological charge. By introducing perturbations, the BIC splits into two circular polarization points with half-integer topological charges, a characteristic that plays a crucial role in chiral applications. In contrast, the GM, with the entire dispersion below the light line and that can no longer radiate into free space, does not have such topological features. Thus, upon transformation into QGM, the far-field distribution across the entire band in the momentum space exhibits linear polarization characteristics.

We further present our investigations with both numerical and experimental results on the comparison between these two types of high-Q resonances, i.e., QBICs and QGMs, with the emphasis on the different Q-factor evolution behaviors of them at different wave vectors. We make use of two geometrically similar binary grating structures on a low-loss lithium niobate on an insulator (LNOI) substrate to demonstrate the difference. Both gratings consist of two dielectric ridges within one unit cell. One is the symmetry-breaking grating (SBG), where a different width is introduced to generate the geometric asymmetry between adjacent ridges. In this structure, the period of the lattice remains unchanged whether or not the width difference is present. The other is the period-doubling grating (PDG), in which the introduction of a nonzero width difference between alternating ridges will result in a sudden doubling of the lattice period. For the SBG with vanishing ridge width difference, the SP-BIC modes are supported at the Γ point, exhibiting the topological feature of polarization singularities with infinite-Q factors. As the wave vector increases from 0, the Q factor decays rapidly. When symmetry breaking is introduced into the structure by using
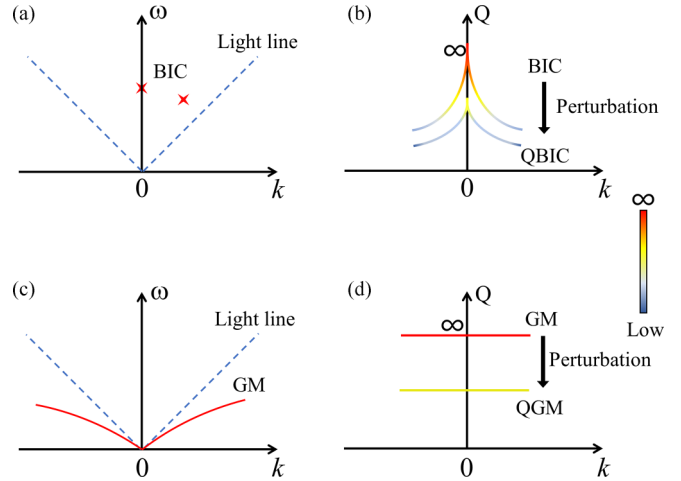

FIG. 1. Schematic figure of BIC and GM dispersions, as well as the Q evolutions at the presence of geometric perturbations. (a) and (c) represent the typical dispersions of two bound modes (BIC and GM) in the energy-momentum space. The blue dashed line represents the light line in air. (b) and (d) describe the dependence of Q factors for different modes as a function of wave vector before and after the perturbation, respectively. The color represents the magnitude of the Q factor.

the width difference, the resulting QBICs still inherit the same trend. In contrast, for the PDG with vanishing period-doubling perturbation, the grating restores to a subwavelength lattice supporting the GMs. With a nonzero perturbation, the GMs will be transformed into QGMs, which exhibit stable Q factors over a wide spectral band and a large range of wave vectors. Although the Q factors of both QBIC and QGMs can be flexibly adjusted by varying the magnitude of perturbation, these two modes retain from their predecessors a different dependence of the Q factors on the wave vector. Some numerical investigations and experimental results are presented to support our statement. These insights into the origin of high-Q resonances in periodic photonic structures will correct the current misunderstanding of the underlying physics in periodic photonic structures and help provide new guidelines for the design of high-Q resonances, which are essential for the manipulation of light-matter interactions using all-dielectric nanostructures.

II. STRUCTURE AND RESULTS

Figure 1 shows schematically the different properties of BICs and GMs, and their derivatives (QBIC and QGM) in the energy-momentum space. According to the topological explanations of BIC [21], the BICs are the singularities in the polarization mapping of the far-field radiations. In other words, they only appear at discrete frequency and wave-vector points within the continuum, i.e., above the dashed blue line of light dispersion in air. As depicted in Fig. 1(a), the two stars denote the existence of two different types of BICs: the left one for the SP-BIC (at $k_x = 0$) and the right one for the accidental BIC, respectively [5]. The SP-BIC can only be located at the Γ point while the accidental BIC happens at the spectral positions where destructive interference occurs between two

radiation channels. Other types of BICs may not be supported by the binary grating structures investigated in this work and thus are omitted for clarity. Taking SP-BICs as an example, they exhibit infinite-Q factors only at the Γ point and the Q factor drops very fast as the wave vector increases from zero [5], as shown in Fig. 1(b). Here we refer to all the high-Q resonances related with BIC as QBIC modes. So, unlike the BICs, the QBICs are not singularity states and have no one-to-one correspondence with the BIC. Even without any geometric redesign, the QBICs can still be achieved by the external perturbation, i.e., using the same structure supporting the BICs but at the wave vectors slightly deviating from that of the BIC [see the top line in Fig. 1(b) or Fig. 4(a) in [5]]. In practical applications, a normal incidence is preferred, and one usually relies on the introduction of geometric perturbations to the structures to transform the SP-BIC into a QBIC state, and then the infinite-Q factor at the Γ point will correspondingly become finite and the vortex point carrying integer topological charges will split into two semi-integer circularly polarized points. As illustrated in Fig. 1(b), a larger perturbation will lead to a further decrease of the general Q factors. Furthermore, the high dependence of the Q factor on the wave vector in the original BIC will be retained in the QBICs, and its high values can only be maintained within a small range of wave vectors near the Γ point due to the dual effects of both the geometric and the wave-vector perturbations. In large contrast with BIC, the GMs in Fig. 1(c) exhibit steep dispersion below the light line. Because the GMs are well-confined modes and their fields cannot escape, they can be considered as having infinite-Q factors and do not have topological characteristics similar to BIC. By varying the wave vector, the corresponding frequency can be significantly tuned, indicating that the infinite-Q factor occurs at any point along the dispersion curve, i.e., within a broad spectral range. When period-increasing perturbations are introduced into the structure, the FBZ shrinks due to the lattice distortion, leading to the folding of GMs above the light line to form new leaky modes (QGMs). As shown in Fig. 1(d), since the QGMs are a derivative of the GMs, the insensitivity of the Q factor to the wave vector is inherited. That means, apart from the possibility of Q-factor control by the magnitude of perturbation, which is the same as the QBIC, all the Q factors of the QGMs at the same perturbation will have the additional asset of high robustness over wave vectors, i.e., the Q factor remains weakly affected by the wave vector. This is very important for many optical applications where one can tune the resonance by varying the incident angle while the Q factor remains almost stable. It is not possible to achieve using the QBIC resonance which, although it can be tuned by varying the incident angle as well, it has the highest Q factor only at a certain wave vector.

To reveal the underlying mechanism in the mode transformations illustrated in Fig. 1 and quantitatively demonstrate the different Q-factor evolution behaviors against wave vectors for QBICs and QGMs, we conducted detailed numerical studies on two binary grating structures. As illustrated in Figs. 2(a) and 2(c), we designed Polymethyl Methacrylate (PMMA) binary gratings with a refractive index of 1.49 on a commercially available z-cut 365-nm-thick lithium niobate (LN) thin film bonding on a 2.5-μm-thick SiO$_2$ buffer on a

quartz substrate. The LN thin film on insulator has become an attractive platform in recent years due to its strong electro-optic effects, providing promising prospects for innovative applications in micro- and nano-optical devices. Importantly, the LN has been considered a key material in the field of nonlinear optics due to its large second-order nonlinear susceptibility $\chi^{(2)}$ and extremely low optical loss from near ultraviolet to mid-infrared region. By carefully designing the structure on this platform, the original one-ridge grating [in Fig. 2(c)] has a period of $P = 410$ nm, and the ridge height and width were chosen as $h = 200$ nm and $w = 150$ nm, respectively. All the length values are constant throughout this work and the only variable to change is the difference δ in ridge width. All the numerical calculations are performed using the commercial software of COMSOL MULTIPHYSICS based on the finite-element method. The numerical models are built with two-dimensional structures, with Floquet periodic boundary conditions applied within the unit cell to the x direction. The Q factor of a resonance observed in the far-field spectrum can be calculated by $Q = \omega_\mathrm{r}/(2\omega_\mathrm{i})$ where ω_r and ω_i are the real and imaginary parts of the obtained complex frequency in the eigenfrequency analysis. Without the loss of generality, we only considered the TE$_0$ mode, with the electric field along the length direction (y) of the ridges. For the SBG shown in Fig. 2(a), which is assumed to have a periodicity of $2P$ to maintain consistency with the PDG, the distance between adjacent grating centers, d, is much smaller than the regular grating period $2P$. A value of $d = 300$ nm is used throughout this work. So, the introduction of the width difference δ, although this breaks the symmetry, does not change the period. When δ vanishes, due to the mirror symmetry across the center of the air gap between the two ridges, the system supports SP-BIC at the Γ point, which is marked by the blue circle in Fig. 2(b). The electric field distribution at this BIC point is presented in the up inset, exhibiting an antisymmetric profile with a zero overlap with the incident plane wave, preventing any in-coupling or out-escaping of the mode, equivalent to an infinite-Q mode. When the perturbation of $\delta \neq 0$ is introduced in the geometry, the asymmetry between the ridge widths leads to the mode distribution slightly away from the antisymmetric profile [although hardly observable from the down inset of Fig. 2(b)] and enables a nonzero coupling with incident plane waves [4], which suggests a switching from the BIC to the QBIC states. As we explained above, the QBICs exist only in a small wave-vector range. For other states along the same dispersion curves but at larger wave vectors, the effect of QBICs fades away. As will be shown later, in that case the background of regular guided mode resonances (GMRs) dominates. In other words, the QBIC are within the same dispersion curves as the background GMRs, but only at small wave vectors. This phenomenon was alternatively interpreted by attributing the symmetry-protected BIC to the coupling between two GMRs [22]. In contrast with SBG, the PDG in Fig. 2(c) exhibits a different behavior. When the width difference between alternating ridges vanishes, the structure restores to a regular grating with a period of P. This subwavelength-period grating supports a set of GMs whose dispersion curve appears below the light line across the whole FBZ in the wave-vector domain $(-\pi/P, \pi/P)$, as shown by the solid blue line in Fig. 2(d).
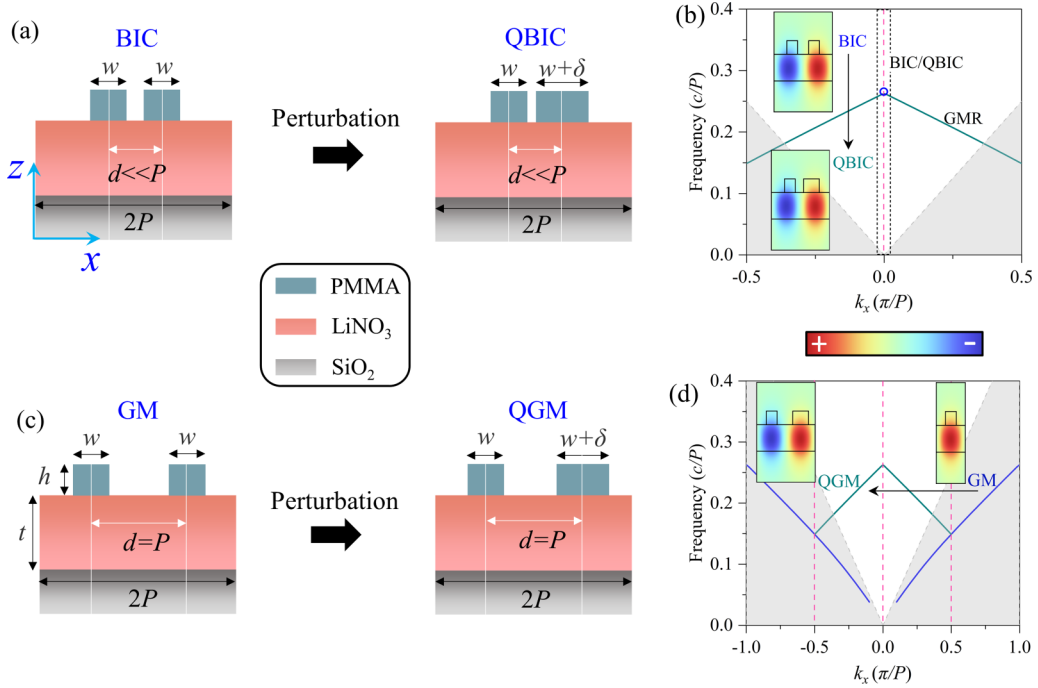
FIG. 2. (a) Schematic diagram of a SBG ($d \ll P$ and the period remains unchanged regardless of δ). When the perturbation of symmetry breaking is introduced, the SP-BIC at the Γ point will transform into a QBIC state. (b) Dispersion structures of the BIC and QBIC/GMR, where the blue circle indicates the position of the BIC and the green lines are the dispersion curves of the QBIC at smaller k_x and the GMRs at large k_x. The insets represent the field distribution of the real part of E_y for both the SP-BIC (up) and the QBIC (down) at the Γ point. (c) Schematic diagrams of a regular grating structure (period: P) and the PDG (period: $2P$). When period-doubling perturbation in the form of width difference between alternating ridges is introduced, the supported GMs transform into the QGMs. (d) Dispersion curves of the original GMs (blue line) and subsequent QGMs (green line), where the insets represent the field distribution of the real part of E_y for GMs and QGMs at the wave-vector positions $k_x = \pi/P$ and $k_x = 0$, respectively.

When a small perturbation δ is introduced between alternating ridges, the period of the photonic lattice is distorted from P to $2P$ and the FBZ shrinks from the original $(-\pi/P, \pi/P)$ to $(-0.5\pi/P, 0.5\pi/P)$. The dispersion of the original GMs is folded at $k_x = \pm 0.5\pi/P$ and the outer side will appear above the light line to form QGMs [see the green line in Fig. 2(d)]. Note that two counterpropagating modes exist both for the GMs and for the QGMs, whose dispersion curves should consist of two branches with a spectral gap. For simplicity, only the lower-frequency branch is plotted here. When δ is much smaller compared to other geometric parameters, the whole system is weakly perturbed. As a result, the QGMs will retain the same shape of dispersion as the GMs, which means

$$f(-k_x) = f(k_x) = f(k_x \pm \pi/P) \approx f_0(k_x \pm \pi/P), \quad (1)$$

where $f(k_x)$ and $f_0(k_x)$ are the dispersion of the QGMs and GMs, respectively. So, in practical applications, the frequency position of QGMs can be directly predicted through GMs to design the structure.

Although the dispersion curves of both the QBICs/GMRs and the QGMs extend to a large proportion of the FBZ [cf. the solid green lines in Figs. 2(b) and 2(d)], the Q factors of the two modes behave distinctly at different wave vectors. Figure 3(a) shows that the Q factors of the BIC/QBIC modes are large only at very small numbers of k_x (close to 0). When $\delta = 0$ nm, as k_x increases, the Q value rapidly decreases from infinity at the Γ point. That is because a nonzero k_x at inclined incidence will work somehow as an extrinsic perturbation

to the whole excitation condition of SP-BIC. At a nonzero δ, which can be considered as an intrinsic perturbation, the SP-BIC transforms into QBIC with a finite-Q factor, but the value still maintains the same decaying trend as a function of k_x as the original BIC. The dependence of the Q factor on k_x at different magnitudes of perturbation is shown in Fig. 3(a). It is seen that the Q value at the Γ point exhibits an inversely quadratic decay relationship with the perturbation δ, which is a well-known behavior of QBICs resulting from the geometric asymmetry [4]. As the wave vector increases, the Q factor drops very fast and gets saturated at the order of 10^3 for relatively large wave vectors ($k_x > 0.02\pi/P$). If no other physics is involved, the Q factor is expected to continue decaying at larger wave vectors. To shed more light on the background Q factor in Fig. 3(a), we designed a control numerical experiment in Fig. 4 using a regular ridge grating with the same ridge-to-period filling ratio as the SBG with $\delta = 0$ in Fig. 3(a). We investigated the GMR Q factor as a function of k_x for a regular grating of the same ridge filling ratio given in Fig. 4(a). The dispersion of the GMR occurring at the second stop band is well known and is plotted in Fig. 4(b), where a SP-BIC state at the upper branch is also marked resulting from an even symmetry across the center of the ridge. Two different behaviors of the Q factors as a function of wave vector are found and plotted in Figs. 4(c) and 4(d) for the two branches of dispersion. Apart from the infinite-Q factor at the SP-BIC state, one can see that the Q factors approach the order of 10^3 at larger wave vectors for both branches. The
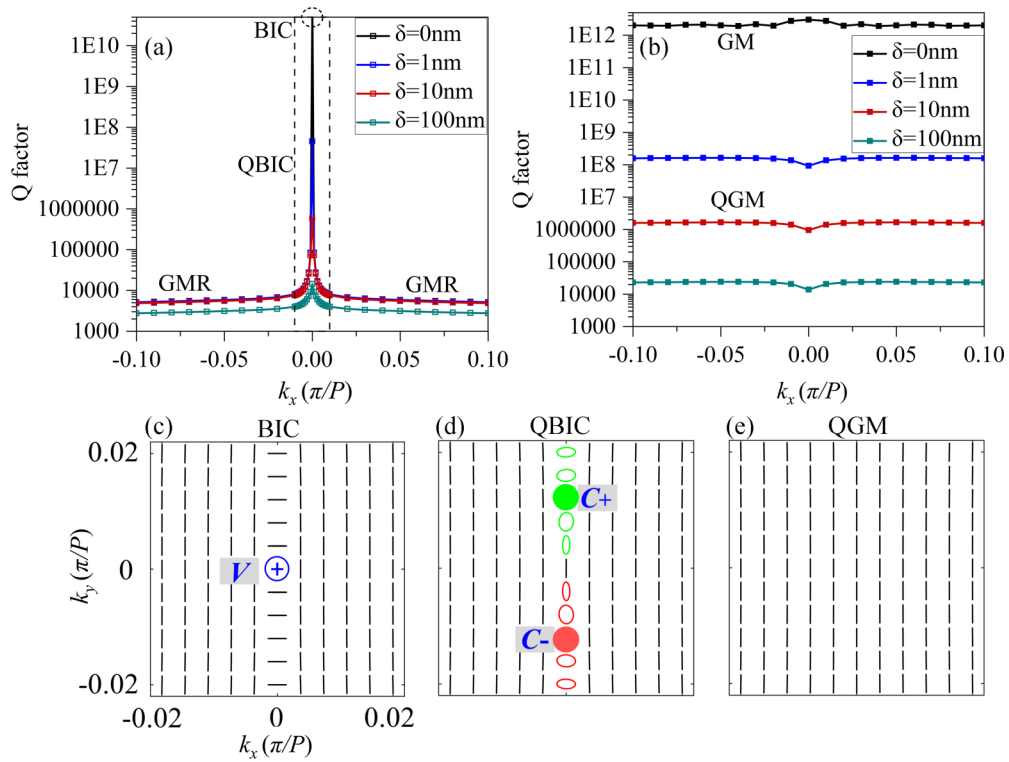
FIG. 3. (a) and (b) show the dependence of Q factor as a function of wave vector at different δ values (0, 1, 10, and 100 nm) for the BIC/QBIC/GMR and GM/QGM systems, respectively. (c), (d), and (e) show the far-field polarization maps near the Γ point for BICs, QBICs, and QGMs, respectively. The blue circle in (c) represents the V point, while the green and red solid dots in (d) represent the positions of the right ($C+$) and left-handed ($C-$) circular polarization points carrying $+1/2$ topological charge, respectively, and the black line in all results represents the linear polarization.

results suggest that the remaining background Q factors in Fig. 3(a) at larger k_x are due to the regularly excited GMRs [23] in the same photonic lattice and has nothing to do with QBIC. Strictly speaking, the modes supported by the SBG

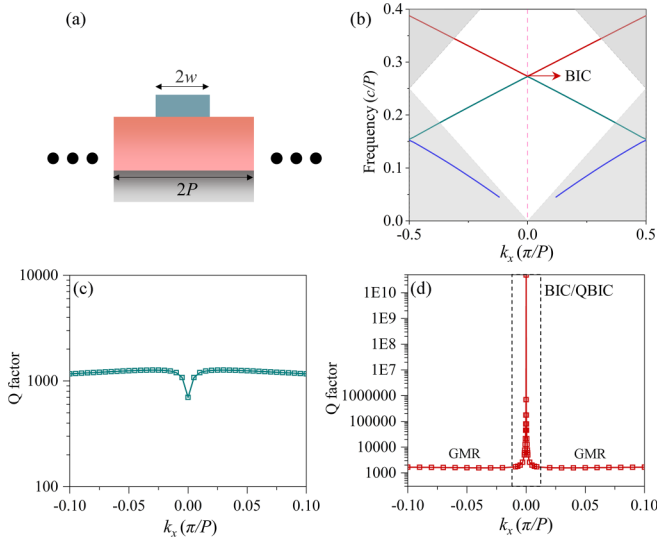

FIG. 4. (a) Schematic diagram of a regular grating (period $2P$). (b) Dispersion curves for the regular grating structure in (a). (c) and (d) illustrate the dependence of the Q factor on the wave vector for the two bands in (b).

structure in Fig. 2(a) can only be claimed as QBICs at small wave vectors along its dispersion in Fig. 2(b) while the rest at larger wave vectors are still GMRs instead, as labeled by the dashed lines in Figs. 3(a) and 4(d). This further confirms our previous statement that the QBICs only occur in a small range of wave vectors.

For the GMs, everything is different. Its dispersion curve exhibits a continuous line shape with an infinite-Q factor along the entire band, as shown by the top line in Fig. 3(b). With the introduction of δ, the GMs transform into QGMs, whose Q factors, although finite, still exhibit a high robustness over the wave vectors. This trend can be found in the lower lines in Fig. 3(b) for different values of δ. As δ increases, the Q factor of QGM at each frequency point also exhibits an inversely quadratic relationship with δ. Importantly, for each δ value, QGM still maintains the robustness of the Q value against k_x. So, the QGM keeps the same advantage as the QBIC that the Q factor can be steered by the magnitude of perturbation and has the superiority that the high-Q factors are not limited to small wave vectors. Both the trend of Q factors for QBIC and QGM as a function of wave vector are consistent with our predictions in Figs. 1(b) and 1(d). Since it is known that the near-field enhancement capability of a resonance is inherently connected to the Q value in the far-field spectrum, the above results of steep QGM dispersion [in Fig. 2(d)] and stable Q-factor values at different wave vectors [in Fig. 3(b)] suggest that it is possible to achieve robust high-Q resonances in terms of broad spectral band and large
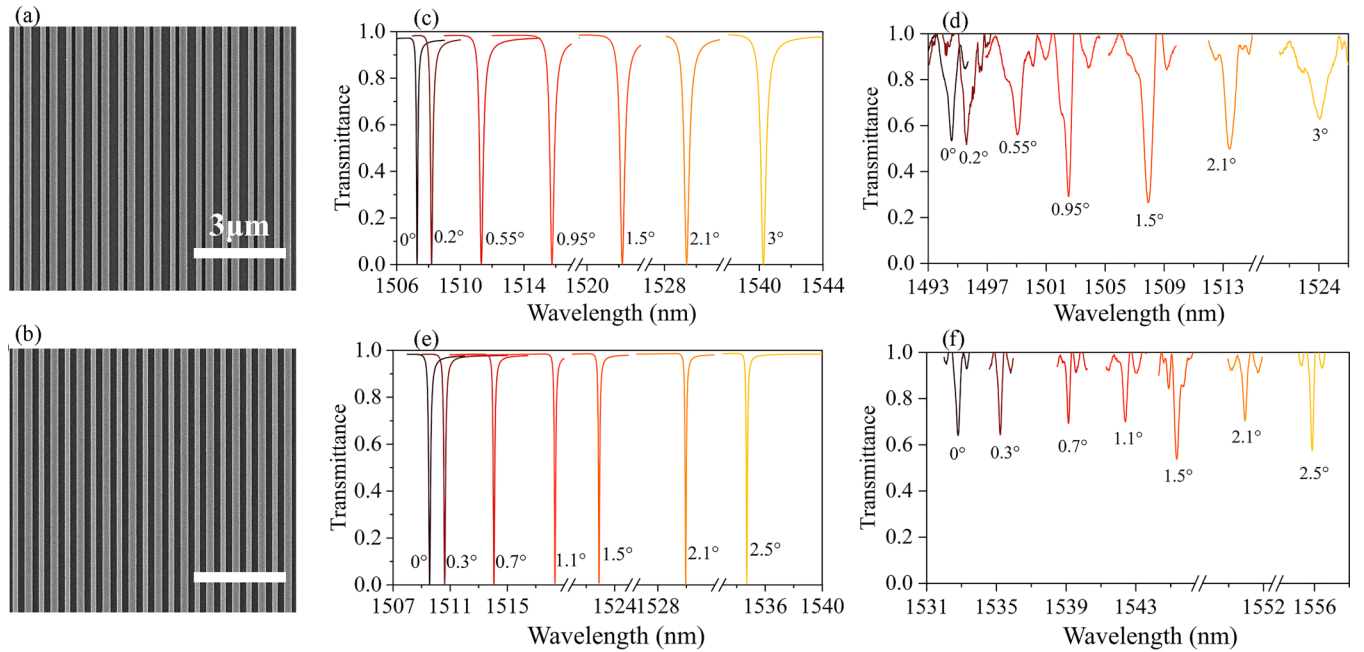
FIG. 5. Top view SEM images for the two binary grating structures of SBG (a) and PDG (b); (c) and (e) The simulated results of the transmittance spectra at randomly selected incident angles for the supported QBICs (c) and QGMs (e), respectively; (d) and (f), the experimentally measured transmittance spectra of the fabricated SBG (d) and PDG (f) samples at multiple incident angles, respectively.

wave-vector range. The spectral tuning can be easily achieved by varying the incident angle, while the Q factors remain unaffected, which is of significant importance for applications such as nonlinear optics with multiple inputs.

Besides the different evolution trends of Q factor as a function of wave vector, we have also investigated the difference between QBICs and QGMs in terms of far-field polarization distributions. It is known that a BIC can be considered as the singularity vortex (V points) in the polarization directions of the far-field radiations [21,24,25]. To characterize the polarization properties of the system, the polarization states of the Bloch mode can usually be mapped onto the Poincaré sphere [26], whose coordinates are specified by the Stokes parameters S_0, S_1, S_2, and S_3. The V points (S_0, S_1, S_2, $S_3 = 0$) usually carry integer topological charges at the Γ point. In the continuum, a nondegenerate eigenmode with an in-plane wave vector k matches only propagating waves with the same in-plane wave vector. The far-field radiation polarization vectors projected onto the xy plane are referred to as $d(\mathbf{k}) = d_x(\mathbf{k})\hat{x} + d_y(\mathbf{k})\hat{y}$. The characteristic of vortices is their topological charge. Here, the topological charge (q) carried by BIC is defined as [21]

$$q = \frac{1}{2\pi} \oint_C d\mathbf{k} \cdot \nabla_k \phi(\mathbf{k}), \qquad (2)$$

where $\phi(\mathbf{k}) = 1/2 \arg[S_1(\mathbf{k}) + iS_2(\mathbf{k})]$ $(-\pi/2 \leqslant \phi \leqslant \pi/2)$ is the orientation angle of the polarization state, and C is a simple closed path in the k space. The calculated V point in Fig. 3(c) corresponds to the SP-BIC supported by the SBG in Fig. 2(a). When the symmetry of the structure is broken (e.g., $\delta = 1$ nm), the SP-BIC transforms into QBICs, where the vortex singularity with an integer topological charge splits into two half-integer circularly polarized singularities (C points) along the symmetry axis, as shown in Fig. 3(d). This feature

has significantly facilitated the research on achieving higher circular dichroism bases on BIC over the past 2 years [27–29]. It can also be seen in Fig. 3(d) that the QBICs with elliptical polarizations only exist within a narrow band of small wave vectors. For larger k_x, all the polarizations switch to linear polarizations along the y direction. This is consistent with our above discussions in Fig. 4(d) that the background Q factors at larger k_x are due to the excitations of GMRs. The far-field polarization of the generated QGMs (at $\delta = 1$ nm) near the Γ point is shown in Fig. 3(e). Different from the QBIC, it is clear that all the QGMs in the k space close to the Γ point have linear polarizations and have no vertexing characteristics at all. This indicates that every resonance in the entire momentum space can be excited by a simple linearly polarized plane wave. The distinct behaviors of the polarization maps close to the Γ point work as a straightforward proof that these two types of high-Q resonances supported by periodic structures originate from different physics.

Following the numerical results, we subsequently fabricated these two geometrically similar binary grating structures of PMMA ridges on an LNOI wafer using electron beam lithography. Due to the limitation in our optical spectrometer resolution, we used $\delta = 80$ nm for both structures. The scanning electron microscope (SEM) images of the two structures are shown in Figs. 5(a) and 5(b), demonstrating excellent fabrication quality. Both the QBIC and the QGM resonances undergo a redshift as the incident angle increases, as the numerical results in Figs. 5(c) and 5(e) demonstrate. This trend is consistent with the dispersions in Fig. 2. We employed a supercontinuum light source with a manual rotation stage to mount the sample to achieve a variable oblique incidence. The details of the fabrication process and the optical measurement setup can be found in the Supplemental Material [30]. The beam diameter of the light source is about 2 mm while the
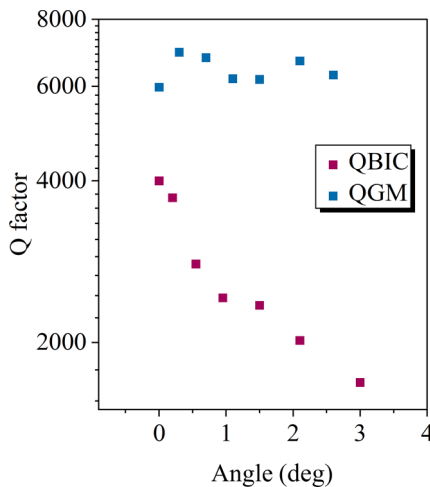
FIG. 6. The Q factors at a function of incident angle, extracted from the transmission spectra in Figs. 5(d) and 5(f).

footprint of both gratings is 5 mm×5 mm. In this case, the incident light from the source can be considered as plane waves with a single wave vector controlled by the incident angle. The measured transmittance spectra at different incident angles for both the QBIC and the QGM resonances can be found in Figs. 5(d) and 5(f). It can be observed that for the QBIC resonances, as the incident angle increases, the resonance expands. This is consistent with our previous discussions, thereby further validating the decaying of the Q factor in the QBIC system when the wave vector moves away from the Γ point. In contrast, the QGM resonances demonstrate almost constant linewidth as the incident angle changes and the resonance shifts, both numerically [Fig. 5(e)] and experimentally [Fig. 5(f)]. To provide a clearer characterization of the changes in linewidth for the two types of quasi bound modes (QBMs), we extracted the Q factors from each transmittance spectrum in Figs. 5(d) and 5(f). Figure 6 shows the dependence of the Q factor on the incident angle for both the QBICs (red) and the QGMs (blue). When the angle increases from 0° to 3°, the Q factor of QBICs rapidly decreases from 4000 to 1600. In contrast, for QGMs, the Q factor remains quite robust with respect to increasing incident angles and stays around 6400. Compared with the calculated results, the slight wavelength mismatch and decrease in Q factor for all the experimental results are mainly attributed to two aspects. Firstly, the slight spectral shift is caused by some fabrication errors, as well as additional optical losses caused by the roughness of the sample surfaces and sidewalls. According to the temporal coupled-mode theory, when these two values of Q_{abs} (contribution from absorption loss) and Q_{rad} (contribution from radiative loss) are equal, the transmittance on resonance reaches zero. The additional losses in the experiment cause a decrease in Q_{abs} and a resultant mismatch of it with Q_{rad}, leading to an increase of the transmittance from zero. Secondly, both the modes exhibit steep dispersion [see Figs. 2(b) and 2(d)]. In actual measurements, the incident beam cannot be plane waves and inevitably contains divergent or focused components. Therefore, when measuring the transmission spectrum at a certain angle, other resonances within the wavelet vector range are simultaneously excited, resulting

in a slight decrease in the Q factor due to the superposition of multiple peaks. However, it is important that these experimental results exhibit exactly the same trend as the theoretical discussion which fully proves our insight in this work into the origin of supported high-Q resonances in periodic photonic structures.

As last remarks in this section, we note that although the regular GMRs can also support high-Q resonances [31], the realization of ultrahigh-Q resonance based on GMRs needs the dimension of the grating elements to be vanishingly small [32,33], which possess either challenges in the fabrication process or limitations in practical applications. Furthermore, the small grating elements indicate that the grating layer itself cannot support well-confined GMs, making the underlayer of an optical slab structure necessary. In contrast, the QGMs do not suffer from such kinds of limitation. A high index contrast grating of subwavelength period without the slab layer can also support well-confined GMs [18,34] and consequently can easily help realize high-Q resonances with high robustness over a large range of wave vectors by harnessing the mechanism of period-changing perturbations.

III. CONCLUSION

In summary, we have demonstrated through detailed numerical and experimental investigations on two geometrically similar binary grating structures, one with a regular symmetry-breaking perturbation and the other with a periodic-changing perturbation, that both structures can support high-Q resonances which originate from two fundamentally different physics instead. The former supports the QBIC resonances whose Q factors decay rapidly as the k values deviate from that of the predecessor BIC, while the latter converts the GMs in the original subwavelength periodic photonic lattices to QGMs. The Q factors of both QBICs and QGMs can be flexibly controlled by the magnitude of perturbations. However, there are distinctions between BIC/QBIC and GM/QGM. The positions of BIC/QBIC remain roughly unchanged in the ω-k space whether the perturbation is present, or not. However, the transition between GM and QGM is accompanied by a swing of the dispersion across the light line. The QBICs inherit the polarization vertexing property of the original BIC and are preferable for light-matter interactions where the spin-optical interactions with matters are involved. The QGMs have another advantage in that the Q factors are more robust against the wave vectors, indicating that one can easily achieve a spectral tuning of the resonance using a single optical geometry while the same level of Q factor as well as the underlying enhanced electric field are maintained. Furthermore, in conjunction with the LN thin-film platform possessing strong electro-optic effects and large second-order nonlinear susceptibility, a constructive approach is provided for the design of multidimensional active optical devices and the generation of spectrally tunable nonlinear optical processes [35].

Our findings in this work shed more light on the underlying mechanism of many high-Q resonances reported in the literature using periodic structures and correct some misunderstandings in this area. We advocate that the nomenclature of the high-Q resonance through perturbing a BM

should be related to its predecessor. In other words, when the perturbation vanishes, the Q factor of the resonance will restore from a finite value to infinity. The essence of the infinite-Q modes should be reflected in the naming of the high-Q resonance. In this context, many high-Q resonances reported in the literature nowadays and claiming to be QBICs are actually QGMs. One typical example is the PCS structure. By changing the size [36,37], orientation [10], or position of the elements [38] in a PCS, the photonic lattice can be affected in either the periodicity in one direction or even the type of lattice [39]. In either case, the lattice distortion will result in a change of the FBZ, and the supported GMs in the original PCS can be engineered correspondingly to become high-Q leaky modes of QGMs. Although the QBICs can indeed be

supported due to symmetry breaking, according to our analysis in this work, only those at a very limited range of wave vectors can be considered as QBICs. While many people seem to use the nomenclature of QBIC all the time, or introduce some concepts like Brillouin zone folding driven bound states in the continuum [40], it is more suitable to use QGMs instead considering that the predecessor of the high-Q resonances in periodic structures is GM, but not BIC.

[1] I. Staude, T. Pertsch, and Y. S. Kivshar, All-dielectric resonant meta-optics lightens up, ACS Photon. **6**, 802 (2019).

[2] L. Huang, L. Xu, D. A. Powell, W. J. Padilla, and A. E. Miroshnichenko, Resonant leaky modes in all-dielectric meta-systems: Fundamentals and applications, Phys. Rep. **1008**, 1 (2023).

[3] T. J. Seok, A. Jamshidi, M. Kim, S. Dhuey, A. Lakhani, H. Choo, P. J. Schuck, S. Cabrini, A. M. Schwartzberg, J. Bokor, E. Yablonovitch, and M. C. Wu, Radiation engineering of optical antennas for maximum field enhancement, Nano Lett. **11**, 2606 (2011).

[4] K. Koshelev, S. Lepeshov, M. Liu, A. Bogdanov, and Y. Kivshar, Asymmetric metasurfaces with high-Q resonances governed by bound states in the continuum, Phys. Rev. Lett. **121**, 193903 (2018).

[5] C. W. Hsu, B. Zhen, A. D. Stone, J. D. Joannopoulos, and M. Soljačić, Bound states in the continuum, Nat. Rev. Mater. **1**, 16048 (2016).

[6] C. Fang, Q. Yang, Q. Yuan, X. Gan, J. Zhao, Y. Shao, Y. Liu, G. Han, and Y. Hao, High-Q resonances governed by the quasi-bound states in the continuum in all-dielectric metasurfaces, Opto-Electron. Adv. **4**, 200030 (2021).

[7] J. von Neumann and E. Wigner, Uber merkwiirdige diskrete eigenwerte, Phys. Z **30**, 465 (1929).

[8] D. C. Marinica, A. G. Borisov, and S. V. Shabanov, Bound states in the continuum in photonics, Phys. Rev. Lett. **100**, 183902 (2008).

[9] I. Deriy, I. Toftul, M. Petrov, and A. Bogdanov, Bound states in the continuum in compact acoustic resonators, Phys. Rev. Lett. **128**, 084301 (2022).

[10] A. Leitis, A. Tittl, M. Liu, B. H. Lee, M. B. Gu, Y. S. Kivshar, and H. Altug, Angle-multiplexed all-dielectric metasurfaces for broadband molecular fingerprint retrieval, Sci. Adv. **5**, eaaw2871 (2019).

[11] K. Sun, M. Sun, Y. Ma, Y. Shi, and Z. Han, Ultra-narrow bandwidth mid-infrared thermal emitters achieved with all-dielectric metasurfaces, Int. Commun. Heat Mass Transf. **143**, 106728 (2023).

[12] K. Sun, Z. Zhao, Y. Cai, U. Levy, and Z. Han, Ultra-narrowband and highly-directional THz thermal emitters based on the bound state in the continuum, Nanophotonics **10**, 4035 (2021).

[13] A. Ahmadivand and B. Gerislioglu, Photonic and plasmonic metasensors, Laser Photon. Rev. **16**, 2100328 (2022).

[14] A. Leitis, M. L. Tseng, A. John-Herpin, Y. S. Kivshar, and H. Altug, Wafer-scale functional metasurfaces for mid-infrared photonics and biosensing, Adv. Mater. **33**, 2102232 (2021).

[15] N. Bernhardt, K. Koshelev, S. J. U. White, K. W. C. Meng, J. E. Fröch, S. Kim, T. T. Tran, D.-Y. Choi, Y. Kivshar, and A. S. Solntsev, Quasi-BIC resonant enhancement of second-harmonic generation in WS$_2$ monolayers, Nano Lett. **20**, 5309 (2020).

[16] Z. Han, F. Ding, Y. Cai, and U. Levy, Significantly enhanced second-harmonic generations with all-dielectric antenna array working in the quasi-bound states in the continuum and excited by linearly polarized plane waves, Nanophotonics **10**, 1189 (2021).

[17] K. Koshelev, S. Kruk, E. Melik-Gaykazyan, J.-H. H. Choi, A. Bogdanov, H.-G. G. Park, and Y. Kivshar, Subwavelength dielectric resonators for nonlinear nanophotonics, Science **367**, 288 (2020).

[18] P. Cheben, R. Halir, J. H. Schmid, H. A. Atwater, and D. R. Smith, Subwavelength integrated photonics, Nature (London) **560**, 565 (2018).

[19] S. Fan and J. D. Joannopoulos, Analysis of guided resonances in photonic crystal slabs, Phys. Rev. B **65**, 235112 (2002).

[20] K. Sun, H. Wei, W. Chen, Y. Chen, Y. Cai, and C. Qiu, Infinite-Q guided modes radiate in the continuum, Phys. Rev. B **107**, 115415 (2023).

[21] B. Zhen, C. W. Hsu, L. Lu, A. D. Stone, and M. Soljačić, Topological nature of optical bound states in the continuum, Phys. Rev. Lett. **113**, 257401 (2014).

[22] P. Hu, J. Wang, Q. Jiang, J. Wang, L. Shi, D. Han, Z. Q. Zhang, C. T. Chan, and J. Zi, Global phase diagram of bound states in the continuum, Optica **9**, 1353 (2022).

[23] R. Magnusson and S. S. Wang, Guided-mode resonance filters, Appl. Opt. **34**, 8106 (1995).

[24] W. Ye, Y. Gao, and J. Liu, Singular points of polarizations in the momentum space of photonic crystal slabs, Phys. Rev. Lett. **124**, 153904 (2020).

[25] J. Jin, X. Yin, L. Ni, M. Soljačić, B. Zhen, and C. Peng, Topologically enabled ultrahigh-Q guided resonances robust to out-of-plane scattering, Nature (London) **574**, 501 (2019).

[26] W. Liu, B. Wang, Y. Zhang, J. Wang, M. Zhao, F. Guan, X. Liu, L. Shi, and J. Zi, Circularly polarized states spawning from bound states in the continuum, Phys. Rev. Lett. **123**, 116104 (2019).

[27] X. Zhang, Y. Liu, J. Han, Y. Kivshar, and Q. Song, Chiral emission from resonant metasurfaces, Science **377**, 1215 (2022).

[28] Y. Chen, H. Deng, X. Sha, W. Chen, R. Wang, Y. H. Chen, D. Wu, J. Chu, Y. S. Kivshar, S. Xiao, and C. W. Qiu, Observation of intrinsic chiral bound states in the continuum, Nature (London) **613**, 474 (2023).

[29] T. Shi, Z.-L. Deng, G. Geng, X. Zeng, Y. Zeng, G. Hu, A. Overvig, J. Li, C.-W. Qiu, A. Alù, Y. S. Kivshar, and X. Li, Planar chiral metasurfaces with maximal and tunable chiroptical response driven by bound states in the continuum, Nat. Commun. **13**, 4111 (2022).

[30] See Supplemental Material at http://link.aps.org/supplemental/10.1103/PhysRevB.109.085426 for details of the fabrication process, the optical measurement setup, additional measured transmission spectra, and the extracted Q values at negative incident angles.

[31] S. S. Wang and R. Magnusson, Theory and applications of guided-mode resonance filters, Appl. Opt. **32**, 2606 (1993).

[32] G. Quaranta, G. Basset, O. J. F. Martin, and B. Gallinet, Recent advances in resonant waveguide gratings, Laser Photon. Rev. **12**, 1800017 (2018).

[33] L. Huang, R. Jin, C. Zhou, G. Li, L. Xu, A. Overvig, F. Deng, X. Chen, W. Lu, A. Alù, and A. E. Miroshnichenko, Ultrahigh-Q guided mode resonances in an all-dielectric metasurface, Nat. Commun. **14**, 3433 (2023).

[34] A. C. Overvig, S. Shrestha, and N. Yu, Dimerized high contrast gratings, Nanophotonics **7**, 1157 (2018).

[35] H. Jiang, K. Sun, Y. Jia, Y. Cai, U. Levy, and Z. Han, Tunable second harmonic generation with large enhancement in a nonlocal all-dielectric metasurface over a broad spectral range, Adv. Opt. Mater. 2303229 (2024).

[36] K. Sun, Y. Cai, U. Levy, and Z. Han, Quasi-guided modes resulting from the band folding effect in a photonic crystal slab for enhanced interactions of matters with free-space radiations, Beilstein J. Nanotechnol. **14**, 322 (2023).

[37] P. Vaity, H. Gupta, A. Kala, S. Dutta Gupta, Y. S. Kivshar, V. R. Tuz, and V. G. Achanta, Polarization-independent quasibound states in the continuum, Adv. Photon. Res. **3**, 2100144 (2022).

[38] A. C. Overvig, S. C. Malek, M. J. Carter, S. Shrestha, and N. Yu, Selection rules for quasibound states in the continuum, Phys. Rev. B **102**, 035434 (2020).

[39] C. W. Neff, T. Yamashita, and C. J. Summers, Observation of Brillouin zone folding in photonic crystal slab waveguides possessing a superlattice pattern, Appl. Phys. Lett. **90**, 30 (2007).

[40] W. Wang, Y. K. Srivastava, T. C. Tan, Z. Wang, and R. Singh, Brillouin zone folding driven bound states in the continuum, Nat. Commun. **14**, 2811 (2023).